J. Fluid Mech. (2005), *vol.* 542, *pp.* 175–194.
doi:10.1017/S0022112005006154 Printed in the United Kingdom

Wavy secondary instability of longitudinal rolls in Rayleigh–Bénard–Poiseuille flows

By HERVÉ PABIOU, SOPHIE MERGUI AND CHRISTINE BÉNARD

Laboratoire Fluides Automatique et Systèmes Thermiques, U M R 7608 (CNRS-UPMC-UPS), Campus Universitaire, 91405 Orsay Cedex, France

(Received 7 December 2004 and in revised form 2 May 2005)

An experimental investigation of the stability of longitudinal rolls in a horizontal layer heated from below in the presence of a Poiseuille flow is carried out. This study follows on from the theoretical work of Clever & Busse (*J. Fluid Mech.*, vol. 229, 1991, p. 517) who detected a wavy instability for a range of relatively low Rayleigh and Reynolds numbers depending on the Prandtl number. In the present study, an air flow is circulating in a rectangular channel of transverse aspect ratio 10 for Rayleigh numbers of 6300 and 9000 and Reynolds numbers from 100 to 174. The system exhibits a wavy pattern only if the flow is continuously excited. The amplitude of the waves grows as they propagate downstream and the frequency of the oscillations is equal to the frequency of the imposed disturbance. The bifurcation from steady longitudinal rolls to unsteady wavy rolls is thus a convective instability. A mode by mode study is performed by measuring the wave velocity and the spatial growth of the instability along the channel for a large range of the imposed frequency. The phase velocity is found to depend only on the Reynolds number, and is nearly equal to the bulk velocity of the flow for all the modes in the range of parameters under study. The maximum spatial growth rate corresponding to the most unstable mode as well as the corresponding frequency decrease with decreasing Reynolds number or Rayleigh number, providing a decrease in the wavelength. This feature is in agreement with the theoretical results of Clever & Busse (1991).

1. Introduction

Stability of convection rolls in a horizontal layer of infinite extent heated from below has been extensively studied by F. H. Busse and co-authors in the 1970s. Many studies have been devoted to the onset of convection rolls in fully developed shear flows and a review of existing work was performed by Kelly (1994). Next, we briefly recall which is the preferred mode of convection arising from the primary destabilization of the basic static state when a laminar flow is imposed on an unstably stratified layer, referred as the Rayleigh–Bénard–Poiseuille (RBP) system in the literature. A linear stability analysis performed by Gage & Reid (1968) showed that the most unstable mode for an infinite layer corresponds to convection rolls aligned with the direction of the flow. For these so-called longitudinal rolls, the critical Rayleigh number is not dependent on the Reynolds and Prandtl numbers, namely $Ra_{cr} = Ra_{cr}(Re = 0) = 1708$, $\forall Pr$. These theoretical results are consistent with experimental studies conducted in channels of large transverse extent for sufficiently high Reynolds numbers (Akiyama, Hwang & Cheng 1971; Ostrach & Kamotani 1975; Fukui, Nakajima & Ueda 1983). However,

the existence of stable travelling convection rolls with axes perpendicular to the flow (transverse rolls) has been detected for low Reynolds numbers and/or narrow channels, due to the presence of lateral boundaries in the system (Luijkx, Platten & Legros 1981; Ouazzani *et al.* 1989; Ouazzani, Platten & Mojtabi 1990). For the longitudinal roll solution, the effect of confinement on the critical value becomes negligible for systems of transverse aspect ratios greater than 5, whatever the Prandtl and Reynolds numbers (Luijkx & Platten 1981).

Linear temporal stability analyses are nevertheless not sufficient to understand the experimental results of Ouazzani *et al.* (1990). Indeed, there is a region in the (Re, Ra)-plane where a laminar Poiseuille flow is observed experimentally whereas transverse rolls are expected from the theory. This contradiction was first removed by Müller, Lücke & Kamps (1992) who investigated the spatial development of disturbances using a weakly nonlinear theory in an infinite layer. A transition from absolute to convective instability was found for the transverse rolls, and the corresponding boundary in the (Re, Ra)-plane moved closer to the separation line between transverse and longitudinal patterns experimentally observed by Ouazzani *et al.* (1990) or calculated by Nicolas, Mojtabi & Platten (1997). A complete review of the literature dedicated to the transverse rolls was recently given by Nicolas (2002). Using a linear analysis based on the study of the system response to an initial impulse, Carrière & Monkewitz (1999) have shown that, unlike the transverse rolls, the longitudinal rolls never become absolutely unstable. Moreover, as long as the flow is convectively unstable, i.e. for a Rayleigh number below the convective/absolute boundary of transverse rolls, the most amplified mode corresponds to longitudinal rolls. Hence, in experiments of sufficiently large transverse aspect ratio and sufficiently high level of noise one should observe longitudinal rolls as long as the nonlinear effects are not significant, which is consistent with the existing experimental investigations.

In the following, the papers mentioned are only concerned with flows in large aspect ratio channels (typically greater than 5) and with uniform imposed temperatures on the top and bottom walls. In physical flows, the longitudinal rolls are always initiated near the sidewalls of the channel and then propagate gradually to the core as the flow moves downstream as can be seen from the visualizations reported in Chang, Yu & Lin (1997), Chang & Lin (1998) or Lir, Chang & Lin (2001) among others. The presence of lateral boundaries in laboratory experiments could thus be considered as a perturbation of an ideal unbounded flow allowing for the spontaneous development of the convective instability. Indeed, in the experiments a conducting state occurs at the lateral walls leading to horizontal temperature gradients. Consequently, a vertical ascending buoyancy-driven flow develops next to the walls giving rise to the onset of the first longitudinal roll as the cold fluid enters the channel. The scenario of roll formation reported in all the experimental studies results in a symmetric pattern and an even number of rolls. A numerical study conducted by Narusawa (1993) showed that the thermal boundary conditions at the inlet or at the walls of the channel play an important role in the number of rolls and in the length needed to obtain a fully developed flow. Prior to the study of Carrière & Monkewitz (1999), many experimental investigations have tried to establish some correlations for the development length of the rolls (Kamotani & Ostrach 1976; Hwang & Liu 1976; Chiu & Rosenberger 1987; Chang *et al.* 1997). Although this quantity is difficult to define and is strongly dependent on the nature and the magnitude of the noise in the facilities, all the results are consistent with the fact that the onset of the rolls moves upstream with increasing the buoyancy-to-inertia ratio, i.e. with decreasing the Reynolds number and/or increasing the Rayleigh number.

In most of the experiments cited above, the longitudinal extent of the heated zone is very limited, and this constrains the investigations to the transient zone. The few experiments that dealt with the fully developed regime report velocity and/or temperature measurements in the longitudinal pattern (Mori & Uchida 1966; Ostrach & Kamotani 1975; Fukui *et al.* 1983; Chiu *et al.* 1987). The only study in the literature specifically devoted to the stability of the longitudinal rolls in a RBP flow is the work of Clever & Busse (1991). Using a linear stability analysis performed for an infinite layer subjected to transverse perturbations, two mechanisms of instability were described: the oscillatory instability for low Reynolds numbers and high Rayleigh numbers, well-known in Rayleigh–Bénard convection (Clever & Busse 1974) and the not so well-known wavy instability also detected in the Couette–Rayleigh–Bénard configuration (Clever & Busse 1992). The authors noted that, in analogy with the Rayleigh–Bénard problem (Clever & Busse 1979), for moderate Prandtl number the skewed varicose instability should be detected before the oscillatory instability by adding relevant perturbations to the system. For higher Reynolds numbers, a wavy pattern is observed with the same properties of symmetry as the oscillatory one but with higher wavelengths in the mean flow direction (typically, for a Prandtl number of 0.7, the critical wavelength is approximately 10 times the height of the channel but only double for the oscillatory instability). At the onset of the instability the most unstable mode is characterized by an infinite wavelength. The minimum Reynolds number for the onset of the wavy instability changes little with the Prandtl number but the minimum of the critical Rayleigh number strongly increases with increasing Prandtl number. The wavy instability is expected to appear for a Reynolds number above about 70 and for a difference between the critical Rayleigh number for the wavy instability and the critical Rayleigh number for the longitudinal rolls of 400 for $Pr = 0.7$ while this difference reaches 4×10^4 for $Pr = 7$. In the latter case the knot instability precedes the oscillatory and the wavy instabilities.

Before this theoretical work by Clever & Busse, unsteady behaviour of RBP flows has been qualitatively invoked in the experimental papers of Avsec (1937), Avsec & Luntz (1937), Bénard & Avsec (1938), with visualizations of wavy patterns in Avsec (1937). Ostrach & Kamotani (1975) mentioned irregularities in air flow for high Rayleigh numbers with an increase in the magnitude of the temperature fluctuations as the Rayleigh number is increased, which should correspond to the skewed varicose or the oscillatory instability. Chiu & Rosenberger (1987) have detected a 'snaking instability' on the longitudinal rolls for low Reynolds numbers and high Rayleigh numbers. More interesting are the unsteady patterns reported by these authors for higher Reynolds numbers (the Rayleigh number is not given) with a perturbation at the inlet of the channel introduced by heating the flow in the entrance zone. This pattern should correspond to the wavy instability, but unfortunately no visualization is available. Chang *et al.* (1997) reported unsteady and asymmetric movements in an air flow at high Rayleigh number and moderate Reynolds number, obviously due to the oscillatory instability that is conveyed by successive merging and splitting of rolls. A snaking vortex flow is observed in the experiments by Chang & Lin (1998), but it also concerns the oscillatory domain of high Rayleigh numbers. The latter studies are well illustrated but nevertheless quantitative data have not been provided.

The aim of this paper is to investigate the wavy instability arising from the destabilization of the longitudinal rolls by an experimental approach. In accordance with the theoretical results of Clever & Busse (1991), experiments are performed using air ($Pr = 0.7$) for which the region of the stable rolls as well as the region of the wavy patterns are large and bounded by moderate values of Rayleigh and Reynolds

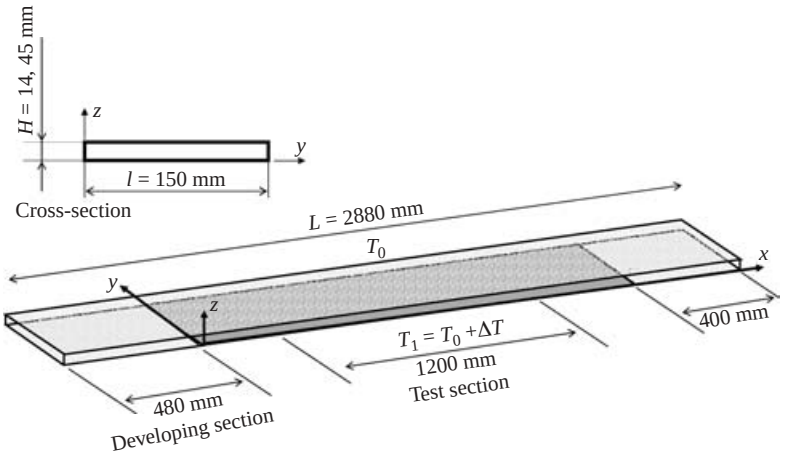

FIGURE 1. Geometry of the experimental setup.

numbers. Accurate visualizations of the flow provide quantitative measurements of the wave velocity and frequency as well as the growth rate of the instability along the channel.

The paper is organized in the following manner. The experimental apparatus is described in § 2. In § 3 are presented the results concerning the nature of the instability, the phase velocity measurements and the spatial evolution of the waves along the channel. Concluding remarks are given in § 4.

2. Presentation of the experiments

2.1. *Experimental setup*

This section provides a description of the apparatus. More details can be found in Pabiou (2003). As shown schematically (figure 1), this apparatus has been designed to generate an air flow in a horizontal differentially heated rectangular channel in order to span the parameter ranges $30 < Re < 300$ and $Ra < 12\,000$. The non-dimensional quantities are calculated using the bulk velocity U_m, the height of the channel H and the vertical temperature difference $\Delta T = T_1 - T_0$. Physical properties are taken at a reference temperature of 20 °C close to the cold temperature T_0. The dimensions of the channel are $L \times l \times H = 2880 \times 150 \times 14.45$ mm, where L, l and H are the length, the width and the height of the channel respectively, providing a transverse aspect ratio $B = l/H = 10.38$. The bottom plate is divided into three regions. A 2 m long central heated region is surrounded by two unheated zones: an upstream development zone of 48 cm sufficient to obtain a fully developed Poiseuille flow at $Re = 300$ and a downstream zone of 40 cm to minimize exit effects. The origin of the x-axis corresponds to the beginning of the heated zone. Figure 2 gives a general view of the experimental setup. The flow rate is regulated at a constant value by a flow controller located ahead of a settling chamber connected to the rectangular channel via a honeycomb structure and a two-dimensional contraction nozzle. The channel lies on a vibration control system to absorb external perturbations. The whole experimental setup is inside a thermal regulated room maintained at a constant temperature around 20 °C.

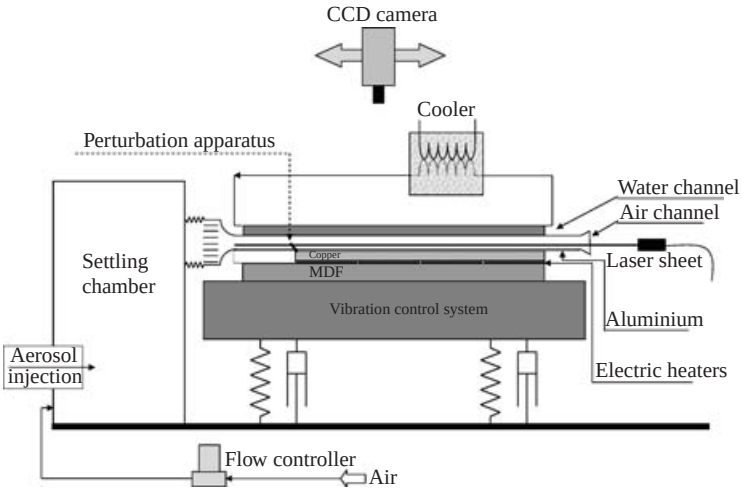

FIGURE 2. Sketch of the experimental apparatus.

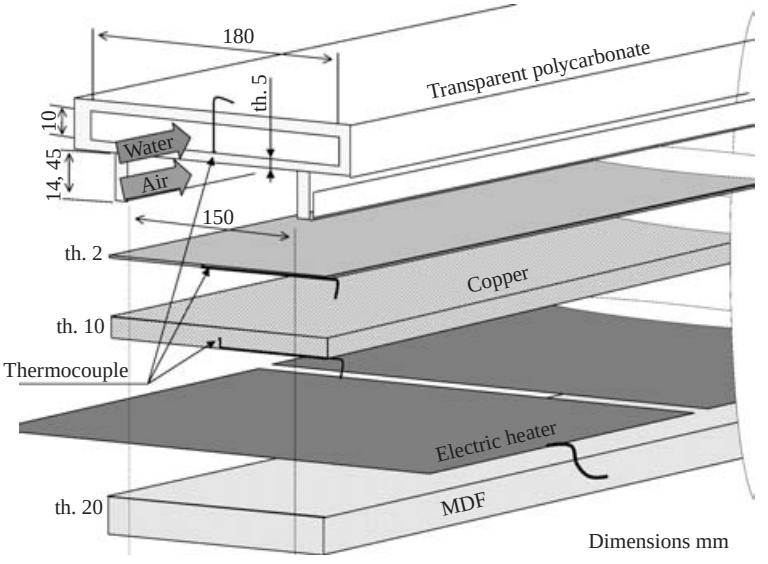

FIGURE 3. Sketch of the channel cross-section (th. stands for thickness).

Flow patterns are visualized using a horizontal laser sheet located at mid-height of the air channel and oil particles injected in the settling chamber using an aerosol generator. Observations are performed using a high-resolution (12-bit) digital CCD camera. Figure 3 shows a sketch of the cross-section of the channel. The cold temperature at the top boundary is maintained constant around $T_0 = 20\,^{\circ}\mathrm{C}$ using water circulation in a transparent channel placed above the air channel. The temperature of the circulating water is measured by five thermocouples distributed on the lower plate of the water channel. The bottom boundary of the air channel is maintained at a constant hot temperature T_1 using electric heaters. The heated section consists of five electric heaters placed between an insulating material board and a 10 mm thick copper plate covered by a 2 mm thick aluminium plate. A closed-loop control is applied to

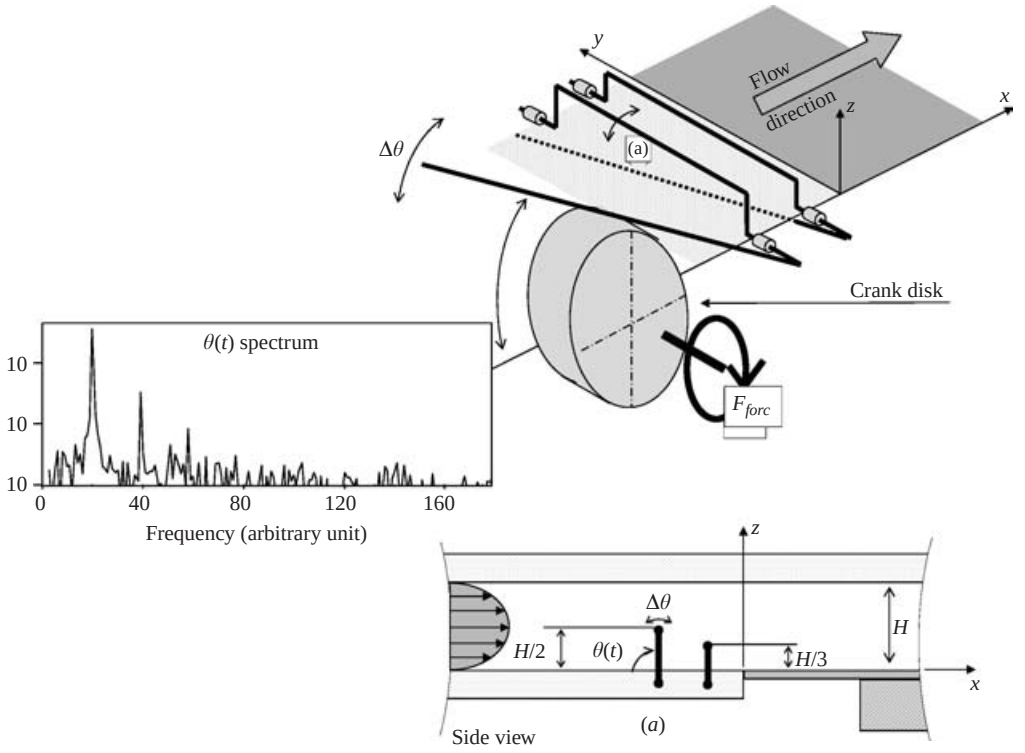

FIGURE 4. Perturbation apparatus located at the inlet of the heated zone and power spectrum of the measured angular displacement $\theta(t)$.

ensure uniform heating along the plate, by measuring the temperature field in the copper medium using 22 thermocouples embedded at mid-height. For each heater, the electrical power is a function of the difference between this temperature field and the desired value. Due to heat losses at the ends of the heated zone, uniformity (in space and time) is achieved within 0.05°C over a central section of 1.2 m defined by $40 \leqslant x \leqslant 160$ cm (figure 1), providing a real longitudinal aspect ratio $A = L/H = 83$. The hot temperature T_1 is measured using eight thermocouples embedded inside the aluminium plate at 0.5 mm from the surface.

The wavy instability is investigated by studying the response of the flow to a disturbance introduced at the inlet of the heated zone. The apparatus represented in figure 4 and located at $x = -2$ cm (figure 2) has been designed to impose a perturbation with a controlled frequency. It is formed by a 1 mm diameter rod parallel to the y-axis over the whole width of the channel and driven by a crank disk. The movement of the rod is characterized by its mean position θ_m and its angular displacement $\Delta\theta$ and is roughly given by the relation

$$\theta(t) = \theta_m + \Delta\theta \cos(2\pi f_{forc} t + \phi), \tag{2.1}$$

where ϕ is a constant. In fact, the angular displacement generated by a crank disk is not perfectly sinusoidal. For our apparatus, the time evolution of the movement of the rod has been recorded using a digital camera to provide the angular position $\theta(t)$. The modulus of the discrete Fourier transform of $\theta(t)$ is shown in figure 4 and one can detect the highest peak linked to the imposed frequency and the first

harmonic. We will see later that the existence of the harmonic, the amplitude of which is one order of magnitude less than the amplitude of the fundamental frequency, has an influence on the observations. For each experiment presented in this paper, the rod labelled (*a*) is used to disturb the flow, the other one being always at rest ($\theta = 90°$).

The flow rate is the sum of the flow imposed by the controller and the aerosol flow. The relative error in the Reynolds number has been estimated by the relation $0.014 + 2.7/Re$. The accuracy of the Rayleigh number values has been evaluated from the errors in the geometry H, and in the hot T_1 and cold T_0 temperatures. The height of the channel in the test section, measured with circulating water in the upper channel, is $H = 14.45 \pm 0.15$ mm. This uncertainty provides a relative error of 6 % in the Rayleigh number. It has been verified that the presence of the air flow (in the Re range studied) has no detectable influence on the temperature measured by the thermocouples embedded in the aluminium plate along the test section. For example, the temperature of the lower plate is $T_1 = 43.02 \pm 0.1\,°\mathrm{C}$ in the case $Ra = 6300$. Concerning the top boundary of the air channel, recall that the polycarbonate wall between the air and the circulating water has a finite thermal conductivity ($0.19\,\mathrm{W\,m^{-1}\,K^{-1}}$). The temperature T_{water} measured in the water channel is thus not a useful measure of the temperature of the upper boundary of the air channel. In order to evaluate the temperature gradient in the polycarbonate wall and thus estimate the real temperature of the upper cold boundary T_0 which is out of reach, the experimental results by Kamotani & Ostrach (1976) have been used. In that study, a heat transfer coefficient between the air flow and the bottom has been found to be within $2 < h_1 < 7\,\mathrm{W\,m^{-2}\,K^{-1}}$ in the range $30 < Re < 1100$ and $10^3 < Ra < 10^4$, when a longitudinal rolls pattern has developed. Assuming that this estimation is valid for the upper plate, the conservation of the heat flux in a one-dimensional model can be written: $h_1(T_1 - T_0) = -(k_{pc}/e_{pc})(T_{water} - T_0)$, where k_{pc} and e_{pc} are the thermal conductivity and the thickness of the polycarbonate plate respectively. From this relation, one obtains

$$0.84(T_1 - T_{water}) < T_1 - T_0 < 0.95(T_1 - T_{water}),$$

and the temperature difference was obtained as follows:

$$\Delta T = T_1 - T_0 = 0.90(T_1 - T_{water}). \tag{2.2}$$

In the following, Rayleigh numbers are calculated using the temperature difference given by equation (2.2). Note that the error associated with this estimation is systematic, and thus will not be included in the error related to the Rayleigh number value. As a consequence, the whole set of results presented in this paper may be shifted slightly along the Rayleigh number axis. The uniformity of the cold temperature field is characterized by the error associated with temperature measurements in the water channel T_{water}. In the case $Ra = 6300$ one obtains a relative error in temperature of 2 % that can be added to the error due to the geometry, providing a relative error on the Rayleigh number value of about 8 %.

2.2. *Experimental protocol*

Measurements of the frequency and of the amplitude of the oscillations at a fixed longitudinal location as well as the wave velocity are performed by image processing. For the frequency and the amplitude, a small region of the flow extending over about five rolls is filmed by the digital camera. A typical snapshot frame is displayed at

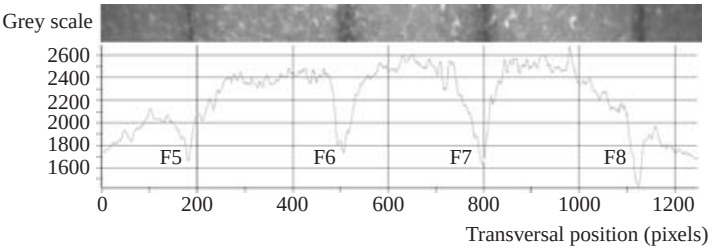

FIGURE 5. Frame extracted from a film and associated mean intensity profile. The dimensions of the physical region are 4×45 mm in the x- and y-directions respectively. Dark lines represent the boundaries between two rolls.

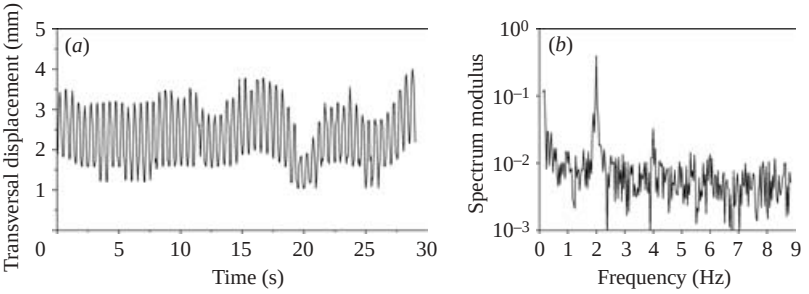

FIGURE 6. (*a*) Time evolution of the transversal displacement of the boundary F5 and (*b*) corresponding norm of the discrete Fourier transform. Longitudinal position $x = 160$ cm, forcing frequency $f_{forc} = 2,0$ Hz.

the top of figure 5 where a dark zone represents a boundary between two rolls. The boundaries of the rolls are labelled from F0 to FN_{roll}, where F0 and FN_{roll} are respectively the right and the left sidewall of the channel when looking downstream. The transversal displacement of a roll can be thus detected by following the time evolution of the position of a dark line at a fixed longitudinal location. The large grey scale of the digital camera allows an accurate determination of the local minima of the intensity profile (dark pixels) as shown in figure 5. Depending on the spatial resolution, boundaries appear as dark strips of 10 to 30 pixels width and their transverse displacements are from about 10 to about 100 pixels. For each film and each boundary, we choose a fixed window containing the displacement of the boundary. Then, the minimum of the raw intensity profile is found inside the window. Figure 6(*a*) shows a signal obtained, together with the modulus of its discrete Fourier transform (figure 6*b*). The predominant peak that appears in figure 6(*b*) indicates that the signal is mono-periodic. The amplitude of this leading mode can be directly obtained from the height of the peak if the duration of the signal is a multiple of the period (Bergé, Pomeau & Vidal 1988). Under this condition, the amplitude is four times the height of the peak. The accuracy of this method is mainly determined by the quality of the films, the size of the corresponding physical region and the frame rate of the camera.

The phase velocity is determined from images of larger longitudinal extent (figure 7*a*) allowing the development of a spatio-temporal representation of the perturbation. At each time step, a fixed horizontal line of pixels that intersects a wavy boundary is extracted from the frame. The spatio-temporal representation is

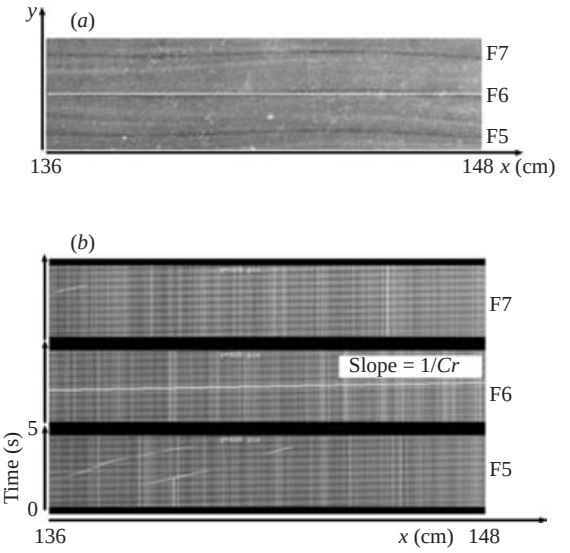

FIGURE 7. (*a*) Frame extracted from a film used for phase velocity measurements. Dimensions of the physical region are 120×80 mm in the x- and y-directions respectively. Dark lines represent the boundaries between two rolls. (*b*) Three spatio-temporal images related to the boundaries F5, F6 and F7. ($Re = 174$, $Ra = 6300$), forcing frequency $f_{forc} = 2,0$ Hz.

constructed by juxtaposing each line in chronological order as illustrated in figure 7(*b*). If the boundary's distortion is due to a sinusoidal disturbance, a set of parallel inclined dark lines will appear on the spatio-temporal image. The slope of these lines represents the wave speed of the perturbation. The wavelength of a given mode is calculated from the wave speed measurement. The ratio between a typical wavelength ($O(10\,\text{cm})$) and the amplitude of the transversal displacement ($O(1\,\text{mm})$) is too high to conduct a direct accurate measurement using an instantaneous image of suitable longitudinal extent.

2.3. *Set of experiments*

In this paper, four sets of parameters are investigated: ($Re = 100$, $Ra = 6300$); ($Re = 120$, $Ra = 6300$); ($Re = 174$, $Ra = 6300$) and ($Re = 120$, $Ra = 9000$). In the (Re, Ra)-plane, these points are located inside the unstable domain predicted by Clever & Busse (1991). For example, for a Rayleigh number of 6300, Clever & Busse (1991) found that the wavy instability occurs for Reynolds number greater than or equal to 65. The point ($Re = 120$, $Ra = 9000$) provides results for a larger Rayleigh number. Moreover the buoyancy-to-inertia ratio $(Ra - Ra_{cr})/Re^2$ is the same for the two cases ($Re = 120$, $Ra = 9000$) and ($Re = 100$, $Ra = 6300$). For each set of parameters, the range of frequencies under study is chosen in order to take into account the most unstable mode.

3. Results

3.1. *The longitudinal rolls*

According to the numerical study of Nicolas, Luijkx & Platten (2000), 10 longitudinal rolls are expected to develop in our channel of aspect ratio $B = 10.38$. In fact, our experimental apparatus provides 10 or 12 rolls depending on the way the experiment is

carried out. When an isothermal Poiseuille flow is heated from below, a 10-roll pattern is always observed. But when differential heating is first applied, then an isothermal (cold) Poiseuille flow is suddenly imposed, the resulting pattern is dependent on the position of the perturbation apparatus described in the previous section. The supports of the horizontal forcing rods located near the sidewalls of the channel provide disturbances of the flow. Bearing in mind that the longitudinal steady rolls are convectively unstable and always develop from the lateral walls, the behaviour of the basic flow, here in terms of number of rolls, is not surprisingly affected by the apparatus even if it is at rest. If the two forcing rods are inside the flow ($\theta = 90°$, see figure 4), 12 longitudinal rolls arise in the channel. If the rods lie on the bottom plate, a 10-roll pattern is observed. Once the thermal equilibrium is reached, no shift from one state to the other has been observed for a given experiment. This result can be explained by the low thermal conductivity of the upper plate of the channel that leads to a cold temperature that is not well-imposed and then to a thermal printing on the wall which tends to maintain the existing pattern. All the results reported in this paper have been obtained with a 12-longitudinal-roll pattern. This configuration is qualitatively more sensitive to the wavy instability than the 10-roll configuration. It should be noted that most of the results of Clever & Busse (1991) are given for a transverse wavenumber of the base solution (longitudinal rolls) $\alpha = 3.117H^{-1}$ corresponding to the most unstable mode whereas in our experiment the transverse wavenumber is $\alpha = 3.63H^{-1}$ (resp. $\alpha = 3.03H^{-1}$) in the 12- (resp. 10-) roll configuration. Moreover, the numerical study dealt with a time evolution of the perturbations in an unbounded flow whereas in our experiments, we observe a spatial growth of the perturbations in a channel of finite extent. These significant differences prevent us from making quantitative comparisons with the results of Clever & Busse (1991).

3.2. *Nature of the instability*

Figure 8(*a*) displays 12 steady longitudinal rolls visualized in the experiment ($Re = 120$, $Ra = 6300$) when the rods of the perturbation apparatus are at rest. A wavy pattern is visualized by applying a permanent excitation to the steady rolls, as illustrated in figure 8(*b*). The rolls oscillate in phase and the amplitude of the oscillations grows along the channel. The same feature is observed for the other points in the (Re,Ra)-parameter space chosen in the unstable domain predicted by Clever & Busse (1991).

Figure 9 displays the time variation of the transverse position of a boundary between two rolls and the magnitude of its spectrum without (figure 9*a*) and with (figure 9*b*) a permanent excitation at frequency $f_{forc} = 2.75$ Hz, for the experiment ($Re = 174$, $Ra = 6300$). Without any imposed perturbation, the signal is characterized by weak and slow variations and no predominant frequency is detected in the corresponding spectrum. The very slow displacements of the boundaries have often been spontaneously observed in our measurements, due to external uncontrolled perturbations that are not filtered by the vibration control system. Although the longitudinal roll are likely to be sensitive to this quasi-steady external noise, this phenomena will not be prejudicial to our study however because the wavy instability is not sensitive to the low-frequency modes as we will see in § 3.4. When the longitudinal rolls are continuously excited with a forcing frequency $f_{forc} = 2.75$ Hz, the signal is sinusoidal, as confirmed by the sharp peak of the corresponding spectrum. Hence, for these two parameters (Re, Ra), the wavy instability needs to be continuously excited to remain in the system. Moreover, the frequency of the leading mode is found to

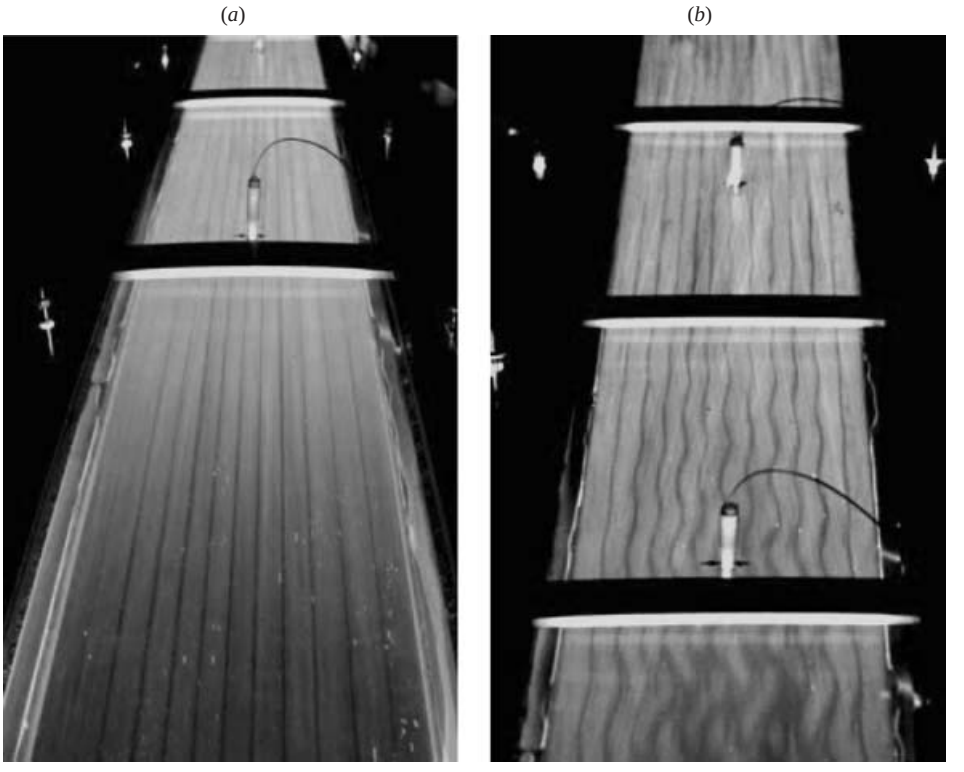

FIGURE 8. Visualization of the flow pattern ($Re = 120$, $Ra = 6300$). The flow comes from the top of the images. (*a*) 12 steady longitudinal rolls are observed without excitation of the flow (*b*) 12 wavy rolls are observed when the flow is continuously excited at the inlet of the heated zone. Dark lines represent boundaries between two rolls.

be equal to the forcing frequency within a resolution of 0.04 Hz. This result holds for almost all investigated modes as shown in figure 10 which displays the oscillation frequency as a function of the imposed frequency for a given boundary. The case of $f_{forc} = 1.0$ Hz which shows a leading mode at 2.0 Hz will be examined in § 3.4. Figure 11 displays the evolution of the amplitude of the oscillations linked with the mode of frequency $f = 2.75$ Hz measured along the heated zone for the boundary $F3$. The amplitude slightly decreases at the beginning of the channel then increases downstream from the location $x = 1.05$ m. In other words, this mode is damped in the first part of the flow then is amplified in the rest of the channel, proving that the longitudinal rolls are unstable at this point. It is believed that the decrease observed in the first part of the channel has a direct bearing on the initial excitation generated by the forcing rod. The perturbation apparatus mainly provides a vertical displacement of the fluid while the resulting wavy instability is characterized by a lateral displacement of the rolls. In other word, the motion generated by the mechanism has a relatively small effect on the shape of the unstable mode and everything orthogonal to that mode shape decays. The development of the damping zone should be affected by changing the properties of the initial signal. Figures 9, 10 and 11 show that the onset of the wavy pattern is obviously the result of the spatial growth of a perturbation in the downstream direction that is continuously introduced at the inlet of the heated zone. The system acts like a noise amplifier, which indicates that the bifurcation from steady longitudinal rolls to unsteady wavy rolls is a convective instability.

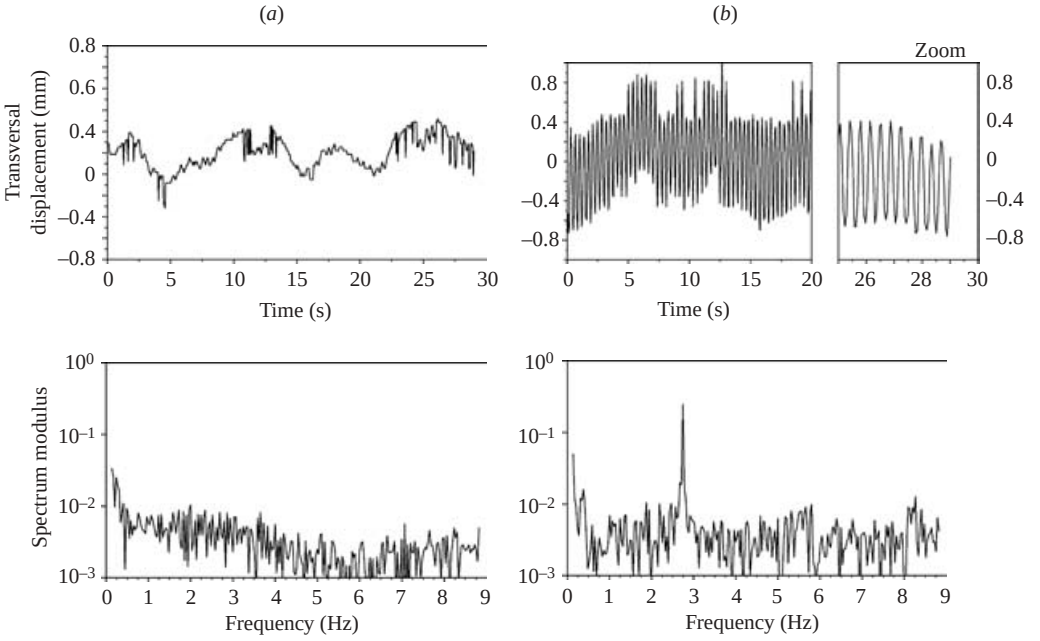

FIGURE 9. Time evolution of the position of the boundary F3 at $x = 1.60\,\mathrm{m}$ and norm of the corresponding spectrum. (*a*) Without excitation, (*b*) continuous excitation at a forcing frequency $f_{forc} = 2.75\,\mathrm{Hz}$ ($Re = 174$, $Ra = 6300$).

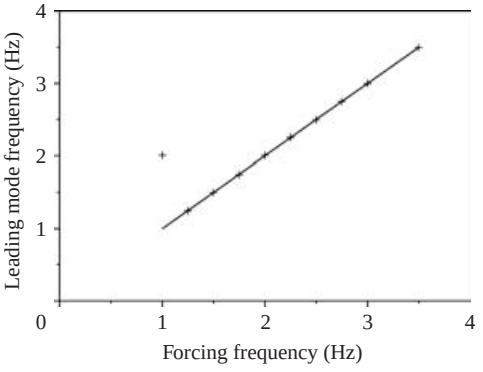

FIGURE 10. Frequency of the leading mode as a function of the frequency imposed at the inlet of the heated zone for the boundary F3, at location $x = 1.60\,\mathrm{m}$ ($Re = 174$, $Ra = 6300$). The slope of the solid line is equal to unity.

To prove this assertion, figure 12 displays the amplitude of the mode of frequency $f = 2.0\,\mathrm{Hz}$ at location $x = 1.25\,\mathrm{m}$ for different values of the angular displacement of the perturbation system. This measurement is for the most unstable case corresponding to the experiment ($Re = 120$, $Ra = 9000$) as will be seen below. For the other (Re, Ra) points, similar results are obtained with a smaller range of $\Delta\theta$. On one hand, $\Delta\theta$ must be large enough to produce detectable oscillations and on the other hand large values are limited by the experimental facilities. For small perturbations, the amplitude of the response is linear with respect to the amplitude of the imposed excitation. In the case

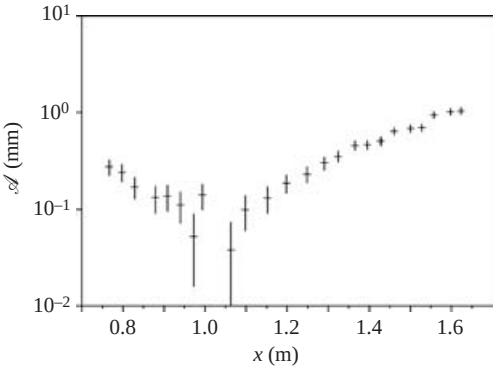

FIGURE 11. Amplitude of the oscillations of the boundary F3 of frequency $f = 2.75$ Hz measured along the test section for a forcing frequency $f_{forc} = 2.75$ Hz ($Re = 174$, $Ra = 6300$).

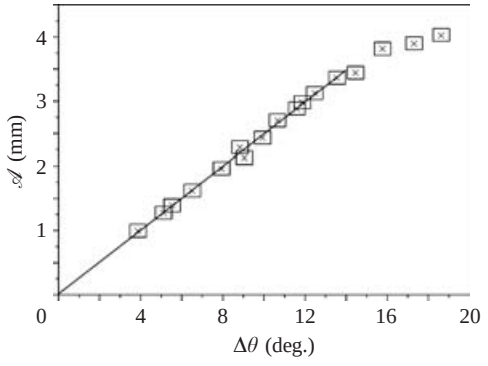

FIGURE 12. Displacement of a boundary between two rolls as a function of the angular magnitude of the perturbation system, at $x = 1.25$ m. The solid line results from a linear regression on the measurements in the linear range. The forcing frequency is given, $f_{forc} = 2.0$ Hz, and the mean value on the angle is estimated at $\theta_m = 80^\circ$ (for notation see equation (2.1)) ($Re = 120$, $Ra = 9000$).

of figure 12, the linear behaviour holds for angular displacements less than 14°. For larger angles, nonlinear effects become significant and the amplitude reaches a finite saturation value of 4 ± 0.5 mm. In an absolutely unstable flow, the amplitude of the resulting perturbation at any location does not depend on the amplitude of the initial perturbation. Figure 12 shows that at a fixed location, for angular displacements less than 14°, the perturbation does not reach its saturated value. Therefore, as the flow is unstable (it will be seen in § 3.4), the flow is convectively unstable.

At ($Re = 120$, $Ra = 6300$) and ($Re = 174$, $Ra = 6300$) the intrinsic noise generated by the experimental facilities is low enough to allow observation of the basic state in the system, but a wavy pattern should occur without applying any perturbation in a longer channel. We will take advantage of this sufficiently low experimental noise to carry out a mode by mode study of this flow. However, a wavy pattern spontaneously arises at the end of the heated zone without additional external perturbation for the point ($Re = 120$, $Ra = 9000$). We will see in § 3.4 that the maximum spatial growth rate of the instability is high enough in this case to allow the intrinsic noise of the apparatus to be strongly amplified and to produce a detectable unsteady pattern at the end of the channel.

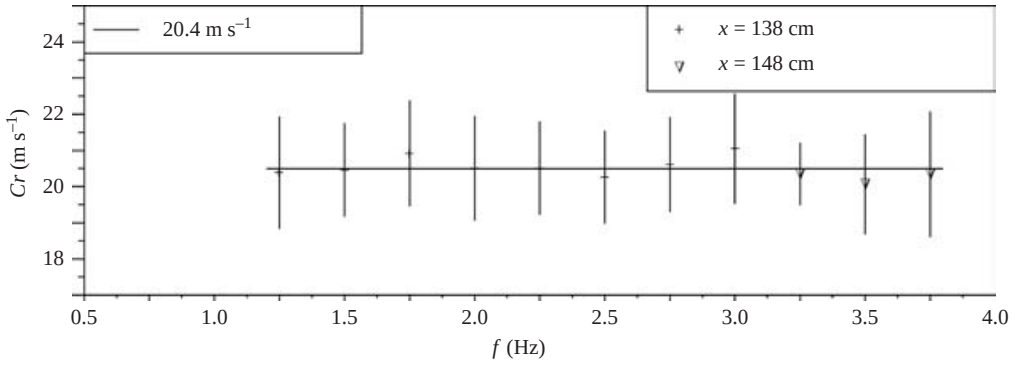

FIGURE 13. Phase velocity measurements at location $x = 1.4$ m for different frequencies. The phase velocity is not dependent on the frequency within $\pm 7\%$ ($Re = 174$, $Ra = 6300$).

3.3. *Phase velocity of the waves*

The phase velocity is measured as described in § 2.2. Figure 13 displays the values obtained for the experiment ($Re = 174$, $Ra = 6300$) as a function of the frequency of the imposed perturbation. In the case reported here and in all our experiments we find that the phase velocity only depends on the Reynolds number. Moreover, the dimensionless value is the same for the three points ($Re = 174$, $Ra = 6300$), ($Re = 120$, $Ra = 6300$) and ($Re = 120$, $Ra = 9000$):

$$Cr = 1.1 U_m \pm 7\,\%. \tag{3.1}$$

For the experiment ($Re = 100$, $Ra = 6300$), the measurements are not easy due to the weakness of the transversal displacement of the rolls leading to a larger uncertainty. These properties of the phase velocity are in agreement with the results given by Clever & Busse (1991) who found that the phase velocity is equal to the bulk velocity within a few percent, not dependent on the Rayleigh number and on the frequency.

3.4. *Spatial growth of the instability*

For the set of parameters considered here, perturbations are small in the first part of the channel and the linear behaviour of the instability previously described in figure 12 is verified. In all our experiments, the latter zone is long enough to carry out a study of the spatial evolution of the perturbation in the linear regime. In fact, the saturation phenomena only occurs in experiment ($Re = 120$, $Ra = 9000$).

According to the linear theory, the growing part of the evolution of the amplitude of the oscillations is described by an exponential function:

$$\mathscr{A}(x) \propto \exp(kx), \tag{3.2}$$

where k is the spatial growth rate; k is found by performing a linear regression on the experimental points x and the logarithm of $\mathscr{A}$. Figure 14 displays this approximated curve for the case presented in figure 11 taking into account the growing part of the evolution only. Using the standard deviation Sd of the residual of the regression, the accuracy of the spatial growth rate is estimated by $k \pm 2Sd/\Delta x$, where Δx is the length over which the measurements are conducted. For the case given in figure 14 the spatial growth rate is 4.0 ± 0.5 m^{-1}.

By varying the frequency of the excitation, the spatial growth rate related to a given boundary is determined for a range of available frequencies as shown in figure 15(a) for the case ($Re = 174$, $Ra = 6300$). The results obtained for all the boundaries under

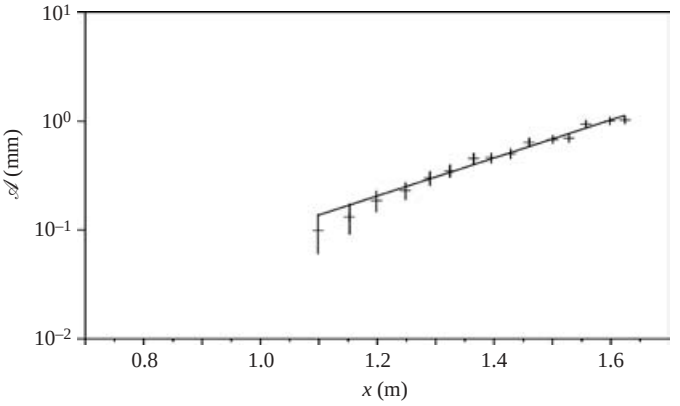

FIGURE 14. Amplification of the oscillations of the boundary F3 along the channel, forcing frequency $f_{forc} = 2.75$ Hz. Experimental points are fitted using an exponential curve given by equation (3.2). ($Re = 174$, $Ra = 6300$).

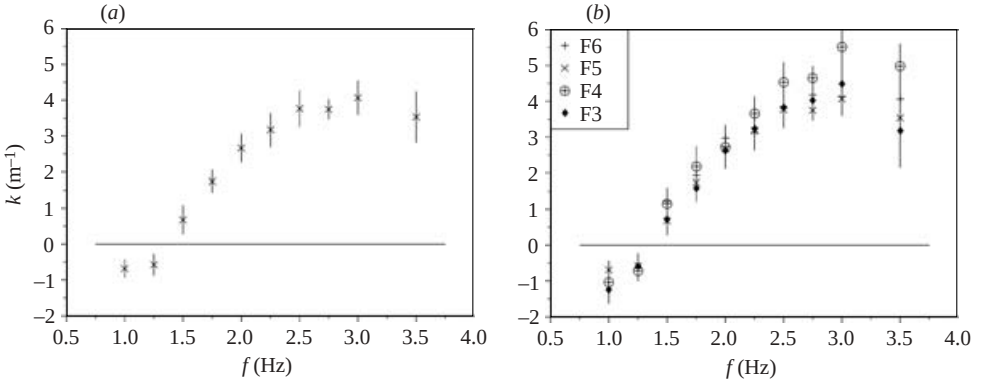

FIGURE 15. Spatial growth rate as a function of the frequency: (*a*) for the boundary F5 and (*b*) for the boundaries F6 F5, F4 and F3. The horizontal line represents the limit of the stability domain $k = 0$ ($Re = 174$, $Ra = 6300$).

consideration are collected in figure 15(*b*). Figure 15(*a*) shows that for boundary F5, the spatial growth rates are positive in the range of frequencies 1.5–3.50 Hz meaning that the corresponding modes are unstable, while the modes of frequencies 1.25 Hz and 1 Hz, with negative growth rates, are stable. Moreover, the points reported in the figure clearly reveal the existence of a maximum in the spatial growth rate distribution, connected to the most amplified mode. For this case, the maximum is $k^{max} = 4.0 \pm 0.5$ m^{-1} corresponding to the mode of frequency $f_{max} = 3 \pm 0.25$ Hz. The discrepancies noted between the boundaries in figure 15(*b*) mostly remain within the error ranges.

As shown in figure 4, the signal generated by the perturbation apparatus is not sinusoidal. For a forcing frequency $f_{forc} = 1$ Hz, the crank disk creates two significant signals at 1 Hz and 2 Hz. For experiment ($Re = 174$, $Ra = 6300$), figure 16(*a*) displays the damping of the fundamental mode $f = f_{forc} = 1$ Hz and figure 16(*b*) displays the amplification of the harmonic $f = 2$ Hz which is compared to the amplification of the fundamental mode 2 Hz measured with a forcing frequency $f_{forc} = 2$ Hz. We note that the spatial growth rates linked to the curves of figure 16(*b*) are equal, providing a good verification of the validity of our measurements.

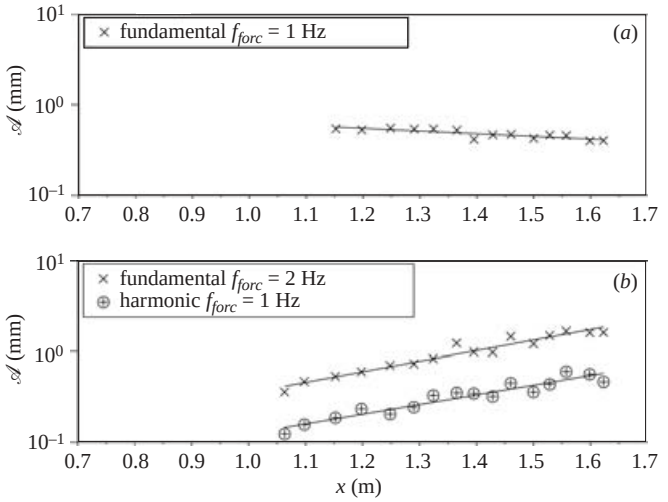

FIGURE 16. Amplitude of the oscillations of the boundary F5: (*a*) damping of the fundamental mode $f = 1$ Hz (forcing frequency $f_{forc} = 1$ Hz), $k = -0.7 \pm 0.3$ m^{-1} and (*b*) amplification of the harmonic $f = 2$ Hz arising from the perturbation apparatus (forcing frequency $f_{forc} = 1$ Hz), $k_h = 2.5 \pm 0.5$ m^{-1}, and of the fundamental mode $f = 2$ Hz (forcing frequency $f_{forc} = 2$ Hz), $k = 2.7 \pm 0.4$ m^{-1} ($Re = 174$, $Ra = 6300$).

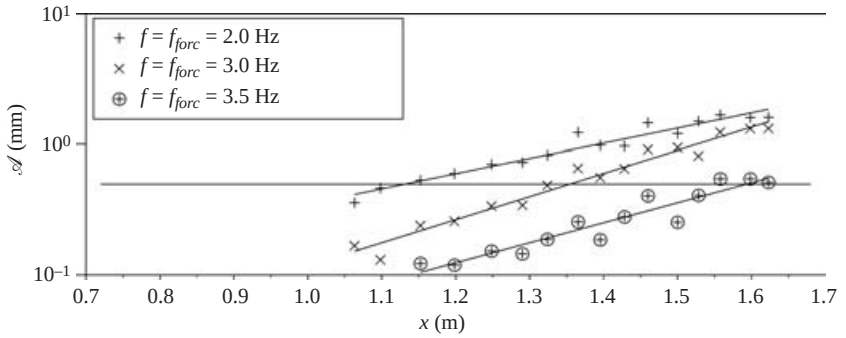

FIGURE 17. Amplitude of the oscillations of the boundary F5 along the channel for three values of the forcing frequency: $f_{forc} = 2$ Hz, $f_{forc} = 3$ Hz and $f_{forc} = 3.5$ Hz. The horizontal line represents an amplitude of 0.5 mm ($Re = 174$, $Ra = 6300$).

We notice that the curve presented in figure 15 is truncated for frequencies above 3.5 Hz. Indeed, beyond this value, the variation in the position of a boundary is no longer detectable. As mentioned in the previous section and displayed in figure 11, the perturbation is damped at first and then amplified to form the wavy pattern. The longitudinal location corresponding to the beginning of the amplification moves downstream as the forcing frequency increases, as illustrated in figure 17 which shows that the longitudinal location corresponding to a given amplitude (here 0.5 mm) is proportional to the frequency. So, for a given experiment, the available range of frequency is bounded, on the one hand due to the finite length of the experimental channel for the higher frequencies and on the other hand due to an amplitude of the oscillations too weak to be detected for the lower ones.

For the case ($Re = 120$, $Ra = 6300$), the curve displayed in figure 18 is more complete with a clear maximum of the growth rate. Indeed, on decreasing the

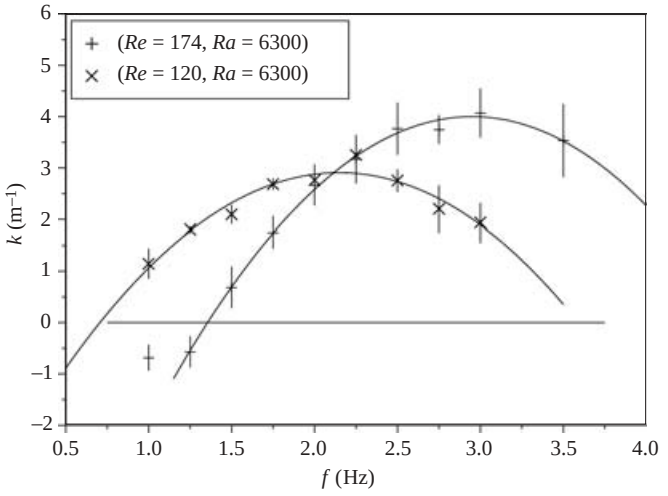

FIGURE 18. Spatial growth rate measured on boundary F5 as a function of the frequency for ($Re = 120$, $Ra = 6300$) and ($Re = 174$, $Ra = 6300$) and approximation with a parabolic curve.

			k^{max} (m^{-1})				
(Re, Ra)	f_{max} (Hz)	λ_{max}/H	F3	F4	F5	F6	F8
(120, 9000)	2.5	3.9					4.6 ± 0.6
(174, 6300)	3.1	4.5	4.1 ± 0.6	5.2 ± 0.5	4.0 ± 0.5	4.2 ± 0.4	
(120, 6300)	2.1	4.6	2.8 ± 0.5		2.9 ± 0.2		
(100, 6300)	1.7	4.8					2.7 ± 0.8
Clever & Busse (1991)							
(162, 3000)	1.7	8.5					

TABLE 1. Most amplified perturbations for the different parameters values. The maximum growth rate and the corresponding frequency are measured from the approximated parabolic curve (see for example figure 18). The accuracy in the determination of the frequency f_{max} is ± 0.25 Hz.

Reynolds number at a given Rayleigh number, the onset of the steady longitudinal rolls moves upstream and for the same magnitude of the inlet excitation, the growing stage of the perturbation is well developed over the length of the test section. The same effect could be achieved by increasing the Rayleigh number at a given Reynolds number.

Figure 18 shows that the maximum spatial growth rate decreases when the Reynolds number decreases from 174 to 120 at a given Rayleigh number ($Ra = 6300$). This trend is in agreement with the linear temporal stability analysis of Clever & Busse (1991) (see their figure 6). Indeed, in the (Re, Ra)-space, the point ($Re = 120$, $Ra = 6300$) is nearer to the neutral curve than the point ($Re = 174$, $Ra = 6300$). A lower Reynolds number should provide a lower maximum growth rate. Nevertheless, the transversal displacements are so weak for the point ($Re = 100$, $Ra = 6300$) ($\leqslant 1$ mm for the most amplified mode), that measurements are not accurate enough to show a significant variation, as can be seen from table 1. But it is clear for the three experiments

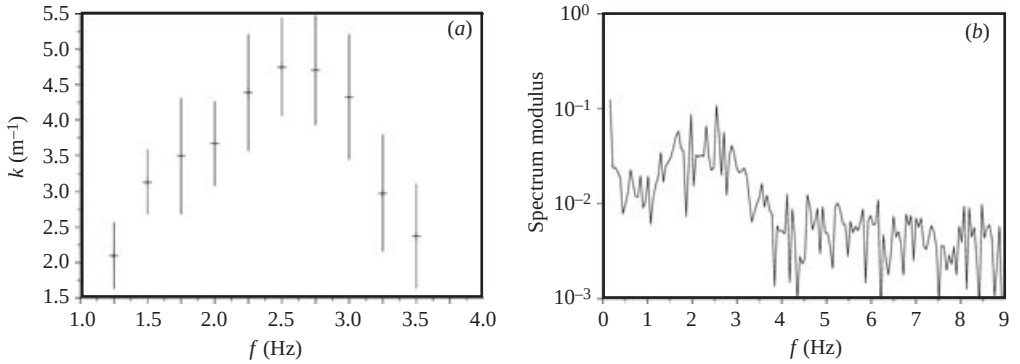

FIGURE 19. (*a*) Spatial growth rate for different modes as a function of the frequency, boundary F8. The most unstable mode is associated with the frequency 2.5 Hz. (*b*) Fourier transform modulus arising from the transversal displacement of the boundary F8 at the downstream location $x = 1.50$ m without imposed perturbation. The frequencies of the unstable modes are in the range 1–4 (*b*). ($Re = 120$, $Ra = 9000$).

conducted at $Ra = 6300$ that the range of unstable modes moves toward the low frequencies with decreasing Re. This feature is consistent with the results of Clever & Busse (1991) concerning the infinite value of the wavelength on the neutral curve. Indeed, the wavelength of the most amplified mode is linked to the phase velocity by $\lambda_{max} = Cr/f_{max}$ with Cr proportional to the Reynolds number. Hence, if the Reynolds number is decreased, it is necessary to detect a large decrease of f_{max} in order to provide an increase of the wavelength. The determination of λ has been performed using this relation and the lack of accuracy associated with the phase velocity measurement yields merely an estimation of the wavelength. The experimental values reported in table 1 show that the trend is however verified. For a given Reynolds number, the maximum spatial growth rate increases with Ra as predicted by the theory of Clever & Busse (1991) and the corresponding frequency provides a decrease in the wavelength. On the other hand, the comparison of the case ($Re = 174$, $Ra = 6300$) with the case presented in the paper of Clever & Busse (1991) ($Re = 162$, $Ra = 3000$) shows that there is a real increase in the frequency of the most amplified mode when the Rayleigh number is significantly increased.

Let us come back to the most unstable case ($Re = 120$, $Ra = 9000$). From figure 19(*a*), we note that the spatial growth rates are positive in the range of frequencies under study, 1.25–3.5. Outside this range, the oscillations are too weak to be accurately measured. The frequency related to the most amplified mode is 2.5 Hz with an estimated error of ± 0.25 Hz. The corresponding value of k gives the maximum spatial growth rate: $k^{max} = 4.6 \pm 0.6\,\mathrm{m}^{-1}$. As mentioned in the previous section, a wavy pattern is spontaneously observed at the end of the heated zone. Without any imposed perturbation, the transversal displacement of the boundary F8 has been recorded at the downstream location $x = 1.50$ m where the saturated zone has been observed. The modulus of its Fourier transform is given in figure 19(*b*). At this location, only amplified modes are detected and the spectrum clearly shows that the frequencies of those unstable modes are inside the range 1–4 Hz, corresponding to the range of unstable modes detected in figure 19(*a*). Due to nonlinear interactions between modes, no dominant sharp peak is detected but the higher ones are quite located around the previous value, 2.5 Hz, associated with the most amplified mode obtained from the mode by mode approach.

4. Concluding remarks

In this paper, experimental work has been developed to trigger an instability detected in a Rayleigh–Bénard–Poiseuille flow by the theoretical work of Clever & Busse (1991) but until now never exhibited in physical flows. The first objective in this study was to create a stable basic state which appears as a longitudinal roll pattern arising from the destabilization of the Rayleigh–Bénard problem. This primary instability is convective and thus depends strongly on the experimental facilities. Our experimental apparatus has been conceived so as to allow the full development of the basic pattern in the range of parameters (Pr, Re, Ra) for which the wavy instability was predicted by the theory. For that, air is used as a working fluid in a channel of height 1.5 cm and width 15 cm, with a heated zone length of 2 m.

The experiments reported in this paper showed that the bifurcation from steady longitudinal rolls to unsteady wavy rolls is also a convective instability which needs to be continuously excited to remain in the channel. The low level of intrinsic noise in the apparatus allowed us to conduct the study in the linear amplification domain and to characterize the behaviour of the instability using a mode by mode approach. For the four experiments presented here, the spatial growth rate of the instability has been determined for all the available modes and the leading mode has been deduced from the detection of the maximum growth rate. The temporal stability analysis of Clever & Busse (1991) provides the dynamical characteristics of the most amplified mode (frequency, phase velocity and wavenumber) but is not able to describe the spatial development of the perturbation.

Experimentally, a more precise analysis of the wavelength behaviour for a wider range of parameters (Re, Ra) is planned in order to try to determine the location of the boundary between the wavy instability and the skewed varicose instability, detected in preliminary experiments performed in our apparatus for moderate Reynolds numbers and sufficiently high Rayleigh numbers. To do that, our intention is to improve the perturbation apparatus in order to generate a transversal excitation of the flow. With this adjustment, we believe that the damping zone of the perturbation detected in the first part of the flow will be reduced while the amplification zone is extended. According to the numerical studies available in the relevant literature, our experimental channel has been designed to minimize the influence of the sidewalls on the onset of the longitudinal steady rolls. But it would be of interest to perform experiments to study how the properties of the wavy instability are affected by the presence of the lateral walls in regard to the unbounded case usually treated in the theoretical works.

REFERENCES

Akiyama, M., Hwang, G. J. & Cheng, K. C. 1971 Experiments on the onset of longitudinal vortices in laminar forced convection between horizontal plates. *J. Heat Transfer* C **93**, 335–341.

Avsec, D. 1937 Sur les formes ondulées des tourbillons en bandes longitudinales. *C. R. Acad. Sci.* **204**, 167–169.

Avsec, D. & Luntz, M. 1937 Tourbillons thermoconvectifs et électroconvectifs. *La Météorologie* **31**, 180–194.

Bénard, H. & Avsec, D. 1938 Travaux récents sur les tourbillons cellulaires et les tourbillons en bandes. Applications à l'astrophysique et à la météorologie. *J. Physique et Radium* **9**, 486–500.

Bergé, P., Pomeau, Y. & Vidal, C. 1988 *L'Ordre Dans le Chaos*, 5th edn. Paris: Hermann.

Carrière, P. & Monkewitz, P. A. 1999 Convective versus absolute instability in mixed Rayleigh-Bénard-Poiseuille convection. *J. Fluid Mech.* **384**, 243–262.

Chang, M. Y. & Lin, T. F. 1998 Experimental study of aspect ratio effects on longitudinal vortex flow in mixed convection of air in a rectangular duct. *Intl J. Heat Mass Transfer* **41**, 719–733.

Chang, M. Y., Yu, C. H. & Lin, T. F. 1997 Changes of longitudinal vortex roll structure in a mixed convective air flow through a horizontal plane channel : an experimental study. *Intl J. Heat Mass Transfer* **40**, 347–363.

Chiu, K.-C., Ouazzani, J. & Rosenberger, F. 1987 Mixed convection between horizontal plates -II. Fully developed flow. *Intl J. Heat Mass Transfer* **30**, 1655–1662.

Chiu, K.-C. & Rosenberger, F. 1987 Mixed convection between horizontal plates -I. Entrance effects. *Intl J. Heat Mass Transfer* **30**, 1645–1654.

Clever, R. M. & Busse, F. H. 1974 Transition to time-dependent convection. *J. Fluid Mech.* **65**, 625–645.

Clever, R. M. & Busse, F. H. 1979 Instabilities of convection rolls in a fluid of moderate Prandtl number. *J. Fluid Mech.* **91**, 319–335.

Clever, R. M. & Busse, F. H. 1991 Instabilities of longitudinal rolls in the presence of Poiseuille flow. *J. Fluid Mech.* **229**, 517–529.

Clever, R. M. & Busse, F. H. 1992 Three-dimensional convection in a horizontal fluid layer subjected to a constant shear. *J. Fluid Mech.* **234**, 511–527.

Fukui, K., Nakajima, M. & Ueda, H. 1983 The longitudinal vortex and its effects on the transport processes in combined free and forced laminar convection between horizontal and inclined parallel plates. *Intl J. Heat Mass Transfer* **26**, 109–120.

Gage, K. S. & Reid, W. H. 1968 The stability of thermally stratified plane Poiseuille flow. *J. Fluid Mech.* **33**, 21–32.

Hwang, G. J. & Liu, C.-L. 1976 An experimental study of convective instability in the thermal entrance region of a horizontal parallel-plate channel heated from below. *Can. J. Chem. Engng* **54**, 521–525.

Kamotani, Y. & Ostrach, S. 1976 Effect of thermal instability on thermally developing laminar channel flow. *J. Heat Transfer* **98**, 62–66.

Kelly, R. E. 1994 The onset and development of thermal convection in fully developed shear flows. *Adv. Appl. Mech.* **31**.

Lir, J. T., Chang, M. Y. & Lin, T. F. 2001 Vortex flow pattern near critical state for onset of convection in air flow through a bottom heated horizontal flat duct. *Intl J. Heat Mass Transfer* **44**, 705–719.

Luijkx, J.-M. & Platten, J. K. 1981 On the onset of free convection in a rectangular channel. *J. Non-Equilib. Thermodyn.* **6**, 141–158.

Luijkx, J.-M., Platten, J. K. & Legros, J. C. 1981 On the existence of thermoconvective rolls, transverse to a superimposed mean Poiseuille flow. *Intl J. Heat Mass Transfer* **24**, 1287–1291.

Mori, Y. & Uchida, Y. 1966 Forced convective heat transfer between horizontal flat plates. *Intl J. Heat Mass Transfer* **9**, 803–817.

Müller, H. W., Lücke, M. & Kamps, M. 1992 Transversal convection patterns in horizontal shear flow. *Phys. Rev.* A **45**, 3714–3726.

Narusawa, U. 1993 Numerical analysis of mixed convection at the entrance region of a rectangular duct heated from below. *Intl J. Heat Mass Transfer* **36**, 2375–2384.

Nicolas, X. 2002 Revue bibliographique sur les écoulements de Poiseuille-Rayleigh-Bénard: écoulements de convection mixte en conduites rectangulaires horizontales chauffées par le bas. *Intl J. Therm. Sci.* **41**, 961–1016.

Nicolas, X., Luijkx, J. M. & Platten, J. K. 2000 Linear stability of mixed convection flows in horizontal rectangular channels of finite transversal extension heated from below. *Intl J. Heat Mass Transfer* **43**, 589–610.

Nicolas, X., Mojtabi, A. & Platten, J. K. 1997 Two-dimensional numerical analysis of the Poiseuille-Bénard flow in a rectangular channel heated from below. *Phys. Fluids* **9**, 337–348.

Ostrach, S. & Kamotani, Y. 1975 Heat transfer augmentation in laminar fully developed channel flow by means of heating from below. *J. Heat Transfer* **95**, 220–225.

Ouazzani, M. T., Caltagirone, J. P., Meyer, G. & Mojtabi, A. 1989 étude numérique et expérimentale de la convection mixte entre deux plans horizontaux à températures différentes. *Intl J. Heat Mass Transfer* **32**, 261–269.

Ouazzani, M. T., Platten, J. K. & Mojtabi, A. 1990 étude expérimentale de la convection mixte entre deux plans horizontaux à températures différentes -II. *Intl J. Heat Mass Transfer* **33**, 1417–1427.

Pabiou, H. 2003 Mise en évidence expérimentale d'une instabilité convective dans un écoulement de Poiseuille-Rayleigh-Bénard. PhD thesis, université Paris VI.